Nanoscale Horizons

Check for updates

Biocompatible cellulose nanocrystal-based Trojan horse enables targeted delivery of nano-Au radiosensitizers to triple negative breast cancer cells†

Giacomo Biagiotti,†[a] Riccardo Cazzoli,‡[bc] Patrizia Andreozzi,[a] Giusi Aresta,[a] Mattii Francesco,[a] Chiara Mangini,[a] Paolo di Gianvincenzo,[d] Chiara Tobia,[e] Sandro Recchia, [ID][f] Laura Polito,[g] Mirko Severi, [ID][a] Orazio Vittorio,[c] Stefano Cicchi, [ID][a] Sergio E. Moya, [ID][d] Roberto Ronca, [ID][e] Adriana Albini,[h] Debora Berti, [ID][a] Roberto Orecchia,[bh] Cristina Garibaldi,*[i] Saverio Minucci‡[bj] and Barbara Richichi [ID]§*[a]

A hybrid cellulose-based programmable nanoplatform for applications in precision radiation oncology is described. Here, sugar heads work as tumor targeting moieties and steer the precise delivery of radiosensitizers, *i.e.* gold nanoparticles (AuNPs) into triple negative breast cancer (TNBC) cells. This "Trojan horse" approach promotes a specific and massive accumulation of radiosensitizers in TNBC cells, thus avoiding the fast turnover of small-sized AuNPs and the need for high doses of AuNPs for treatment. Application of X-rays resulted in a significant increase of the therapeutic effect while delivering the same dose, showing the possibility to use roughly half dose of X-rays to obtain the same radiotoxicity effect. These data suggest that this hybrid nanoplatform acts as a promising tool for applications in enhancing cancer radiotherapy effects with lower doses of X-rays.

New concepts

A programmable cellulose-based hybrid nanoplatform (CNC-AuNPs) for applications in precision radiotherapy for cancer treatment has been developed. The cancer homing ability of the sugar heads makes the cellulose-based nanomaterial a Trojan horse, ensuring a massive and selective accumulation of the Au radiosensitizer in the radioresistant triple negative breast cancer using a low amounts of Au in the treatment. Notably, our Trojan horse approach (i) overcomes the main current limits of the use of the Au radiosensitizer in radiotherapy and (ii) results in augmenting radiotoxicity towards cancer cells using roughly half dose of X-rays to obtain the same radiotoxicity effect. The tumor targeting strategy of our nanotechnology impacts a hallmark of cancer. Thus, our insights open a new route to use such nanotechnology as the nano-radiosensitizer in the treatment of different radioresistant and challenging solid tumors.

[a] *Department of Chemistry 'Ugo Schiff', University of Firenze, Via della Lastruccia 13, 50019 Sesto Fiorentino, Firenze, Italy. E-mail: barbara.richichi@unifi.it*

[b] *Department of Experimental Oncology, European Institute of Oncology (IEO), IRCCS, 20141 Milan, Italy*

[c] *School of biomedical sciences, UNSW Sydney, Kensington, NSW, Australia*

[d] *Soft Matter Nanotechnology, Center for Cooperative Research in Biomaterials (CIC biomaGUNE), Basque Research and Technology Alliance (BRTA), Paseo de Miramon 194, 20014, Donostia-San Sebastián, Spain*

[e] *Experimental Oncology and Immunology, Department of Molecular and Translational Medicine, Viale Europa 11, 25123 Brescia, Italy*

[f] *Department of Science and High Technology, University of Insubria, Via Valleggio 11, 22100 Como, Italy*

[g] *National Research Council, CNR-SCITEC, Via G. Fantoli 16/15, 20138 Milan, Italy*

[h] *Scientific Directorate, IEO, IRCCS, 20141 Milan, Italy*

[i] *Unit of Radiation Research, IEO, IRCCS, 20141 Milan, Italy. E-mail: cristina.garibaldi@ieo.it*

[j] *Department of Oncology and Hemato-Oncology, University of Milan, Milan, Italy*

† Electronic supplementary information (ESI) available. See DOI: https://doi.org/10.1039/d4nh00042k

‡ G.B. & R.C. equally contributed to this work.

§ S.M. & B.R. are co-senior authors.

Introduction

Since the discovery of the therapeutic potential of X-rays, the field of radiation therapy in oncology has witnessed significant advances.[1] Today, radiotherapy (RT) stands as one of the mainstream therapeutic regimens to treat solid tumors, employing technologically advanced machines, improved dose fractionation regimens, and synergistic therapeutic approaches.[1,2] RT harnesses high-energy radiation to trigger cellular damage thus killing cancer cells or slowing their growth by damaging their genetic materials leading to tumor shrinkage. To reach a favorable trade-off between tumor control and toxicity of the surrounding healthy tissues (*i.e.* therapeutic ratio), the RT dose is prescribed to the tumor volume, with the goal of controlling the disease while respecting normal tissue tolerance levels. Recent insights into the radiobiology of tumors and normal tissues have led to innovative strategies aimed at optimizing the radiation therapeutic ratio.[3] However, the challenge of

radioresistant tumors persists as does the requirement for efficient sparing of the surrounding healthy tissues.[3,4] Numerous efforts have been directed towards enhancing tumor radiotoxicity through targeted radiation delivery and tumor-specific sensitization.[3,5,6] In particular, radiation absorbers have been intensively investigated to maximize the radiation dose deposition at the tumor site thereby allowing to use lower and safer radiation doses for non-target tissues (resulting in the same antitumor effect). This approach may also result in an increase of the therapeutic effect for radioresistant tumors while delivering the same dose. Although the concept of radiosensitizers holds great promise, the precise accumulation of a therapeutic radiation dose in cancer cells, the use of a minimal dose of the radiosensitizer in the treatment and its targeted delivery into cancer cells are still unmet needs that significantly affect translational research and limit the application in clinics.

Nanotechnology can face this challenging task, providing integrated nanostructured platforms capable of precise delivery of therapeutics.[7,8] Harnessing multifunctional nanoparticles to ensure a bench-to-bedside perspective requires a thorough control of factors, *i.e.* nanoparticle composition, morphology, manufacturing process and the fate in biological systems.[9] In addition, the attachment of multiple cargos to the nanoparticle surface introduces complexity (*i.e.* time and cost consuming step-by-step protocols and low yield purification procedures) and it is often a crucial bottleneck that significantly affects scalability and formulation uniformity across batches. Concerning the specific application to radiotherapy, gold nanoparticles (AuNPs) thank to higher energy absorption coefficients with respect to soft tissues are excellent radiation absorbers and provide X-ray dose local accumulation in the targeted cells.[10–14] However, the fast turnover of AuNPs (*i.e.* a low driving force for their uptake and rapid clearance), along with the need of a huge dose of AuNPs in the treatment limit bench-to-bedside perspective.

In view of all these considerations, in this work, we provide a conceptual advance in the field. Accordingly, a straightforward

methodology that allows accessing to an original, modular and functional hybrid glyconanomaterial, named **CNC-Au-LA 1** (Fig. 1A), has been recently described.[15] The functional glyconanomaterial is made up of small-sized AuNPs equipped with a lipoamide (LA) spacer and embedded within a cellulose nanocrystal (CNC) matrix. This unique structure allows for easy postfunctionalization with various headgroups, by exploiting a robust click chemistry route. In particular, we demonstrated that the conjugation of sugar heads on CNC-AuNPs **2–3** (Fig. 1A) preserves binding to human carbohydrate-binding receptors.[15] These results have prompted targeting specific receptors on cancer cells.

In this work, we investigate the biomolecular recognition properties of our glyconanomaterial in the context of radiotherapy to specifically maximize the radiation dose deposition in cancer cells, leveraging the presence of AuNPs in CNC-Au-LA. In particular, this study focuses on triple negative breast cancer (TNBC),[16,17] selected as a typical radioresistant cancer model to provide a proof of concept for the technology proposed. TNBC cells are characterized by the lack of the expression of specific targetable receptors that are commonly found in other types of BC. Accordingly, the GLUT channel[18,19] and the mannose receptor[20] were selected in this work as targets widely overexpressed in various tumor types including TNBC. First, we enhanced the colloidal stability of our hybrid glyconanomaterial by increasing the sulphation degree of the pristine CNC, obtaining the **CNC*** (Fig. 1B). Thereby, the new hybrid nanoplatform **CNC*-Au-LA 4** was used as the template to prepare the glucose and mannose functionalized glyconanomaterials **5** and **6** (Fig. 1B), and we investigated the ability of the sugar heads as tumor targeting moieties thus steering the precision delivery of AuNPs into TNBC cells (Fig. 1C). This 'Trojan horse' approach promotes specific internalization and significant accumulation of AuNPs in TNBC cells, thus avoiding the fast turnover of small-sized AuNPs and the need to use high doses of the radiosensitizer for the treatment. Then, leveraging the synthetic
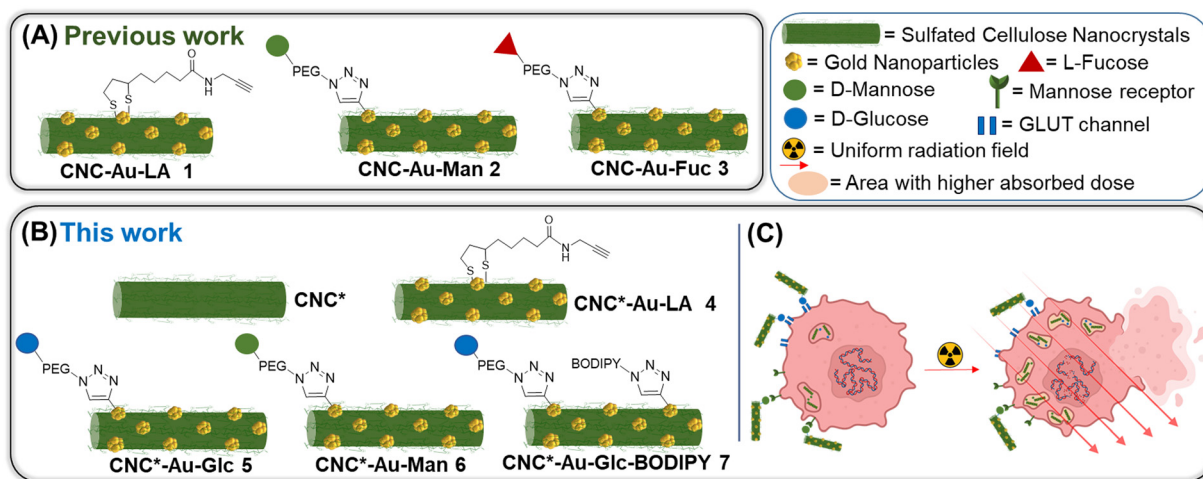

Fig. 1 Schematic representation of the glyconanomaterials described (A) in our previous work and (B) in this work. (C) Schematic representation of the main aim of this work.

flexibility of this approach, we also prepared fluorescently labelled conjugate 7 (Fig. 1B), which enabled following the fate *in vitro* of this glyconanomaterial.

Results and discussion

Synthesis and chemical–physical characterization of glyconanomaterials 4-7

The commercially available sulfated CNC (see ESI†) was used as the template for the preparation of the CNC*-AuNPs conjugates **5–7** (Scheme 1). Sulfate groups play a crucial role in the physiochemical and biological properties of the CNC.[21] The sulfation degree (DS, see ESI†) modulates water dispersibility and consequently the colloidal stability of the CNC dispersions. With this in mind, we increased the DS of the template under controlled reaction conditions. A protocol for gram-scale sulfation of the pristine CNC using a sulfur trioxide pyridine complex in dimethyl sulfoxide (DMSO) was optimized (see ESI†) affording pure **CNC*** with high batch-to-batch reproducibility (Scheme 1A).

The reaction was performed at 25 °C to avoid depolymerization side reactions. **CNC*** was then treated with a NaOH solution to obtain the more dispersible sulfate sodium salt and purified by dialysis. Elemental analysis confirmed the absence of nitrogen as a proof that all the reagents were removed (Table S1, ESI†). The DS was assessed according to a previously reported method[22] (see ESI†) and it resulted 4.3 times higher than the pristine CNC (0.12 of **CNC*** *vs.* 0.028 of the pristine CNC, Table S2, ESI†). Notably, the increase of the DS did not impact significantly on neither the ζ-potential (-44 ± 1 mV for the **CNC*** *vs.* -38 ± 1 mV for the pristine CNC Table S2, ESI†) nor the rod shaped structure of the resulting **CNC*** as observed by atomic force microscopy (AFM) imaging (Fig. 2A). The hydrodynamic size of the dispersion was also determined with dynamic light scattering; data analysis showed a narrow size distribution centered around 130 nm (Fig. 2B). Then, AuNPs bearing the lipoamide spacer **8** (Scheme 1A) were prepared *in situ* using the **CNC*** as the template by following our recently reported one-pot protocol (see ESI†).[15] The increased DS
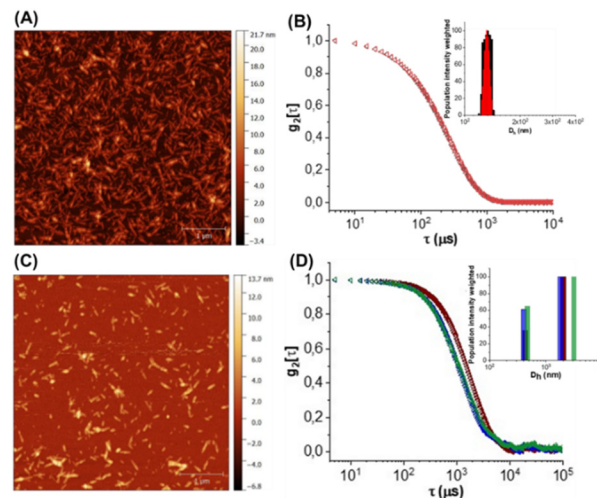

Fig. 2 (A) 5 µm × 5 µm AFM image of the **CNC*** suspension in H_2O dried on mica. (B) Autocorrelation functions of the CNC (black) and **CNC*** (red) dispersed in MilliQ water. Top right size populations overlay (weighted on the scattered light intensity contribution) obtained through Contin's fitting. (C) 5 µm × 5 µm AFM image of the **CNC*-Au-LA 4** suspension in H_2O dried on mica. (D) Autocorrelation functions of **CNC*-Au-LA 4** (brown), **CNC*-Au-Glc 5** (blue), and **CNC*-Au-Man 6** (green) dispersed in MilliQ water. Top right size populations overlay (weighted on the scattered light intensity contribution) obtained through double exponential fitting on autocorrelation functions.

of the **CNC*** did not impart the Au loading of the resulting **CNC*-Au-LA 4**, estimated by inductively coupled plasma atomic emission spectroscopy (ICP-AES) and it consisted of 9.9% w/w (99 µg mg^{-1} as calculated on at least three replicates, Table S1, ESI†). The loading of the spacer **8** was assessed by elemental analysis to be $12.4 \pm 0.8\%$ w/w (0.051 ± 0.003 mmol of **8** over 100 mg of **CNC*Au-LA 4**, based on the nitrogen content on at least three replicates, Table S1, ESI†). In addition, AFM images (Fig. 2A and C) showed that this synthetic step does not bring significant changes in terms of size and polydispersity to those observed for the **CNC***. Moreover, transmission electron microscopy (TEM) analysis confirmed the presence of small sized AuNPs (a mean Au core diameter of around 2.5 nm) with a narrow size distribution (Fig. S1, ESI†). The analysis, with the Porod approximation, of
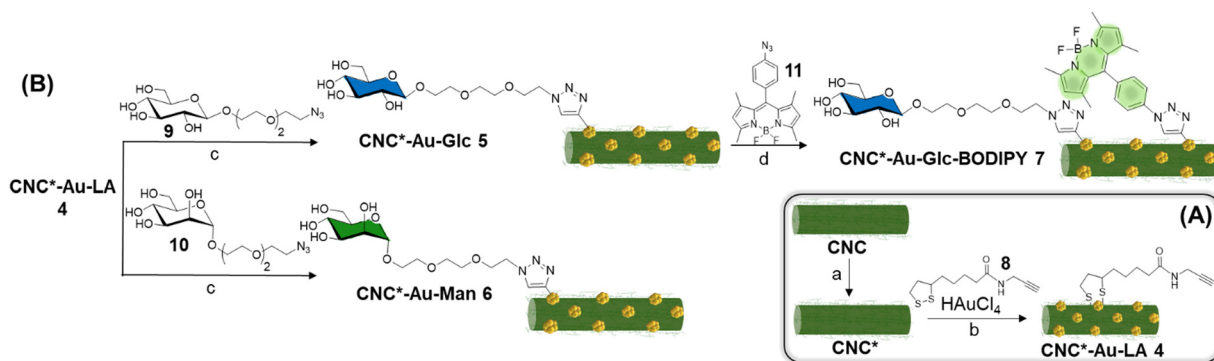
Scheme 1 (A) Synthesis of **CNC*-Au-LA 4**. Reaction conditions: a. Sulfur trioxide pyridinium complex, dimethyl sulfoxide, 4 h, 25 °C; b. HAuCl$_4$, NaBH$_4$, water:methanol (1 : 9), and **8**. (B) Synthesis of **CNC*-Au-Glc 5**, **CNC*-Au-Man 6**, and **CNC*-Au-Glc-BODIPY 7**. Reaction conditions for c and d: CuSO$_4$, sodium ascorbate (water for c and DMF for d), overnight, room temperature.

the SAXS profile obtained for the **CNC*-Au-LA 4** (Fig. S2, ESI†) identifies a trend of I(Q) proportional to $Q^{-2.5}$. This parameter denotes the presence in dispersion of structures with a fractal nature intermediate between that of objects with an extended planar structure (thin sheet like) and three-dimensional organisation.[23] This result is in agreement with the literature, as it is possible to model individual CNC as parallelepipeds, which interact with each other by growing isodesmically to form planar clusters. On the other hand, the three-dimensional contribution identified by Porod's coefficient, is due to the interaction between the dispersing clusters.[24]

Then, β-glucoside **9**[25,26] and α-mannoside **10**[25,26] (Scheme 1B) bearing a PEGylated linker at the anomeric position were reacted with the alkyne residues on the **CNC*-Au-LA 4** surface using a controlled Cu(ɪ)-catalyzed azide–alkyne cycloaddition (CuAAC) reaction in H_2O using a 2 : 1 glycosides to the LA ratio. The CuAAC reactions were repeated at least in triplicate affording the functionalized glyconanomaterials **5** and **6** with high batch-to-batch reproducibility. The loading of the sugar heads was calculated by elemental analyses based on the nitrogen content of **5** and **6** compared with the precursor **CNC*-Au-LA 4** (0.73% w/w in **4** vs. 1.28% w/w in **5** vs. 1.25% w/w in **6**, ESI,† Table S1, ESI†) that resulted in, respectively, 0.015 mmol of **9** and **10** over 100 mg of respectively **5** and **6** (Table S1, ESI†). Then, the ICP-AES analysis confirmed that the functionalization process did not affect the gold loading (Table S1, ESI†). A comparative DLS analysis of glyconanomaterials **4–6** was performed (Fig. 2D); data analysis does not highlight any significant changes in the dimensions of **CNC*-Au-LA 4** nanocrystals post-functionalization with the sugar heads.

Then, fluorescently labelled glyconanomaterial **7** was prepared using an iterative step-by-step conjugation route. Accordingly, **CNC*Au-Glc 5** was further conjugated to BODIPY **11**[27] in DMF (Scheme 1B) affording **CNC*-Au-Glc-BODIPY 7**. The loading of BODIPY **11** was estimated by UV–Vis spectroscopy (λ_{max} = 502 nm, Fig. S3 and S4, ESI†) using the molar extinction coefficient of BODIPY **11** in DMSO (Fig. S4, ESI†) and resulted in 0.5% w/w. The excitation with UV-light (λ_{max} = 480 nm) of **7** resulted in a fluorescence emission peak at λ = 513 nm (Fig. S5, ESI†).

Biological evaluations on TNBC and immortalized (untransformed breast cells) models.

The resistance of TNBC cells to radiation is linked to relatively slow-cycling of the tumor cells and a well-conserved DNA repair machinery, which allows the damage caused to the DNA by the radiation to be effectively repaired.[28,29] In this work, the MDA-MB-231 and MCF10A cell lines were selected as respectively the TNBC model and immortalized, untransformed breast cells (used as a proxy to "normal" cells) to test the efficacy of the approach in circumventing resistance and to provide a proof of concept of the usefulness of the technology proposed in a radioresistant cancer type.

Cell viability without X-rays

MDA-MB-231 tumor cells and MCF10A immortalized breast cells have been used to test the overall cytotoxicity of glyconanomaterials **5–6** after 24 h treatment (Fig. S6, ESI†). The cell

viability has been assessed using a cell titer glo kit (Promega). In the absence of X-ray irradiation, CNC*-AuNPs conjugates **5–6** show low to no effect on cell viability on both cell lines up to a concentration of 50 μg mL^{-1}, with a mild toxicity (around 20% reduction) on MDA-MB-231 at the highest tested concentration of 100 μg mL^{-1}.

### CNC*-AuNPs conjugates are efficiently internalized in TNBC cells *in vitro*

MDA-MB-231 cells were treated with increasing concentrations of glyconanomaterials **4–6** (2.5, 5, 10 and 20 μg mL^{-1}) and the extent of NPs internalization was assessed over time (3.5, 8 and 24 h) by measuring the gold content of cell lysates by ICP-MS (Table S3, ESI†). Fig. 3 shows an increase over time of the gold content on cell lysates with all the glyconanomaterials assayed and a peak upon 24 h. Notably, the dose of 10 μg mL^{-1} (green bar, Fig. 3A) of **CNC*-Au-Glc 5** resulted in a 2-fold increase of Au uptake in MDA-MB-231 cells compared to **CNC*-Au-LA 4** after 24 h of treatment (39.60 ± 3.83 μg L^{-1} gold for **CNC*-Au-Glc 5** vs. 22.40 ± 9.48 μg L^{-1} gold for **CNC*-Au-LA 4**). These results confirmed that the sugar heads play a crucial role in the uptake of the AuNPs on cancer cells. To compare the effect of Au internalization on healthy cells, MCF10A cell lines were treated under the same conditions with increasing concentrations of **5–6**. Notably, after 24 h (dose: 10 μg mL^{-1}), a significant lower uptake of AuNPs in the MCF10A cell line compared to TNBC cells was observed (61% less for **5** and 63% less for **6**, Table S3, ESI†).

Then, we investigated the kinetics of the uptake of the glyconanomaterials in living MDA-MB-231 cells. The glucose bearing conjugate **5** was selected as a model compound and the corresponding bifunctional labelled derivative **7** was used for this purpose. Time-lapse optical microscopy was used to show the dynamic uptake of **CNC*-Au-Glc-BODIPY 7** in MDA-MB-231 cells over 24 h (Video S1, ESI†). The conjugate **7** entered cells after around 16 hours, reaching a steady state afterwards. NP clusters of different sizes were present, heterogeneously distributed throughout the cells, with larger clusters visually resembling membrane-enclosed endosomes. Then, to further evaluate the role of the sugar heads in the cell uptake, the bifunctional labelled derivative **7** was used in a competition assay with the antibody targeting the GLUT1 channel (see ESI†). The cotreatment of MDA-MB-231 with a dispersion of **CNC*-Au-Glc-BODIPY 7** and the anti-GLUT1 antibody significantly reduced the nanoparticle uptake (Fig. S7, ESI†). Indeed, a strong reduction of the green fluorescence associated with glyconanomaterial **7** was observed when the anti-GLUT antibody interacts with the target channel (Fig. S7, ESI†). Further investigations are needed to better characterize the mechanism of the internalization and subcellular localization of the nanoparticles. According to these data, a treatment timeframe of 24 h was selected for the following further studies of radiotoxicity.

Glyconanomaterials 5 and 6 are able to enhance the effect of X-rays irradiation on TNBC cells and do not affect immortalized breast cells

The ability of the CNC*-AuNPs conjugates to increase X-rays irradiation-induced mortality in MDA-MB-231 cells was assessed,
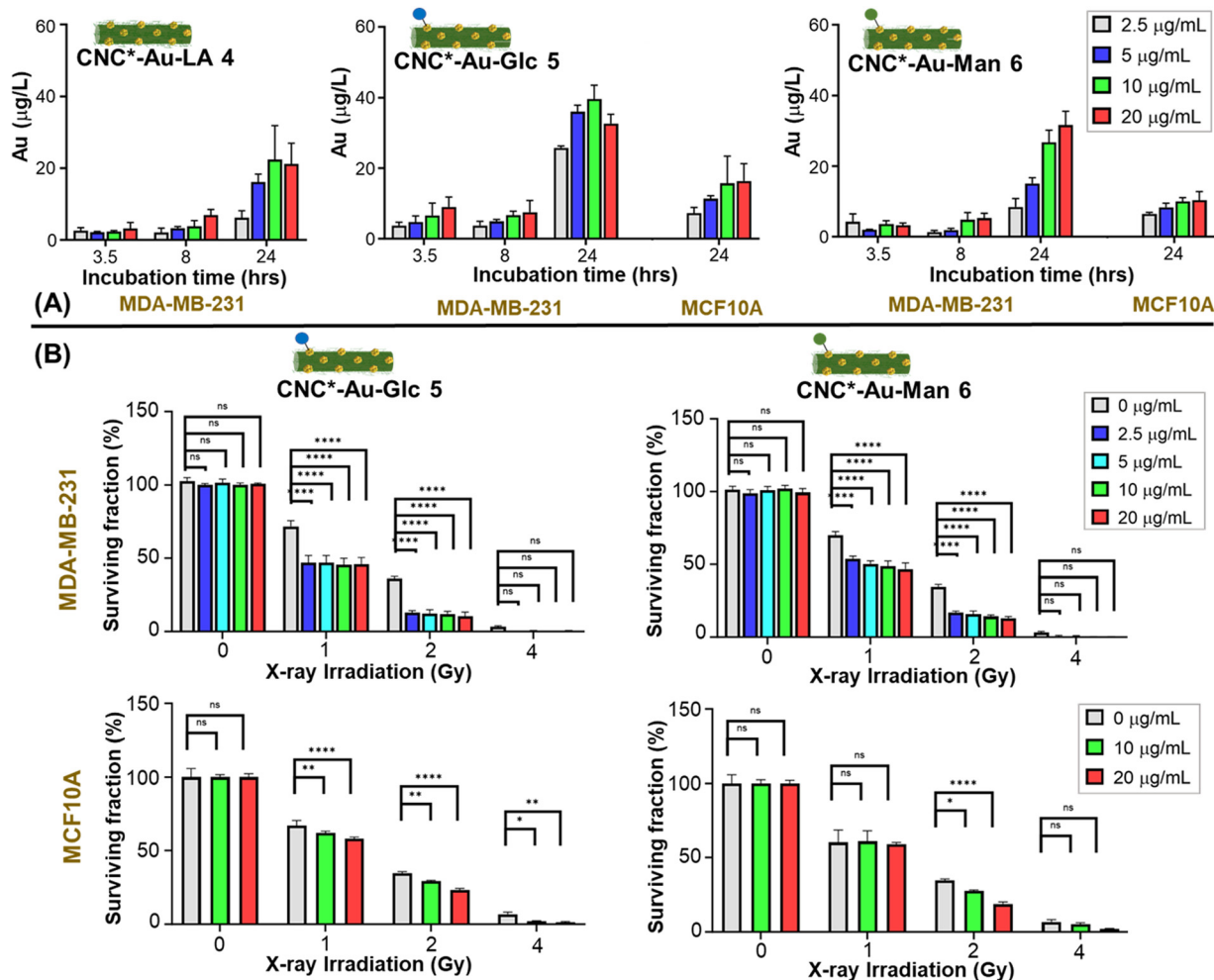
Fig. 3   (A) Cellular uptake of glyconanomaterials **4–6** at different time points and in different cell lines: *i.e.* **CNC*-Au-LA 4** in MDA-MB-231 and **CNC*-Au-Glc 5** and **CNC*-Au-Man 6** in MDA-MB-231 (triple negative breast cancer model) and MCF10A (immortalized breast cells). The error bar indicates the standard deviation from the mean of three replicates (*n* = 3). (B) Surviving fraction of colonies from MDA-MB-231 (upper panels) and MCF10A (lower panels) cells, after combinatory treatment of X-rays and **CNC*-Au-Glc 5** (left) or **CNC*-Au-Man 6** (right). Cells have been exposed to X-rays with or without the glyconanomaterials and then replated at low density immediately after. Colonies have been counted 14 days after irradiation. Data from 2 independent experiments and 2 replicates each (*n* = 4).

and MCF-10A cells were used as the control to assess the specificity of the treatment. Tumor cell responses to damage induced by X-rays can vary from DNA damage checkpoint activation and cell cycle arrest up to induction of senescence and/or cell death. The fate of cells depends on both the intensity and the duration of X-ray exposure, and on cell intrinsic characteristics, such as the ability to repair damages and activate/deactivate cell cycle checkpoints and induced death pathways.[30] Short term assays (24 h after irradiation) can elucidate the effect of X-rays irradiation with/without nanoparticles. In some cases, tumor cells can recover from this state thereby restoring their cell cycle. For this reason, evaluating the long-term ability of cells to form colonies after X-rays treatment is crucial to provide a deeper understanding of the long-term radiotoxicity effect. Then, quantification of the effect of the radiosensitizers in terms of dose enhancement is mainly defined by the dose enhancement factor (DEF),[31,32] which corresponds to the ratio of the radiation dose deposited in

tumors treated with and without a specific radiosensitizer[33,34] (*i.e.* a DEF value of 2 results in the same antitumor effect using half dosing regimens). Accordingly, the DEF values were calculated to obtain a quantitative measurement of the effect. Cells were treated with glyconanomaterials **5** and **6** for 24 h and then exposed to X-rays and the short-term effect on cell viability was evaluated by counting cells 24 h post-irradiation (Fig. S8 and S9, ESI†). Then, the long-term effect was also investigated by measuring the ability of irradiated cells to continue proliferating in colonies when replated (clonogenic potential assay) 14 days post-irradiation (Fig. 3B, and Fig. S10, ESI†). The treatment of MDA-MB-231 cells (Fig. S8 and S9, upper panels, ESI†) with **5** or **6** and irradiated with X-rays resulted in a significant decrease of cell viability compared to cells treated with only X-rays, thus confirming the capacity of the AuNPs to increase the radiotoxicity effect. Indeed, as an example in a short term, the radiotoxicity with an absorbed dose of 2 gray (Gy) in the presence of the CNC*-AuNPs

Table 1 Au uptake (µg L^{-1}, 24 h) in MDA-MB-231 and MCF10A cells and DEF values. MDA-MB231 (top part of the table) or MCF10A (bottom part of the table). Au uptake in cell (µg L^{-1}) columns refer to Fig. 3A data and are reported as value ± SD

CNC*-Au conjugates dose (µg mL^{-1})	Au dose (µg mL^{-1})	CNC*-Au-Glc 5		CNC*-Au-Man 6	
		DEF	Au uptake (µg L^{-1})	DEF	Au uptake (µg L^{-1})
MDA-MB-231					
2.5	0.25	1.74	25.79 ± 0.54	1.45	8.43 ± 2.37
5	0.5	1.77	36.01 ± 1.86	1.59	15.13 ± 1.62
10	1.0	1.82	39.60 ± 3.83	1.65	26.76 ± 3.34
20	2.0	1.77	32.67 ± 2.62	1.72	31.66 ± 3.94
MCF10A					
10	0.25	1.12	15.35 ± 7.76	1.02	10.01 ± 1.08
20	0.5	1.24	16.04 ± 4.92	1.04	10.36 ± 2.46

conjugates gave the same killing effect than obtained with an absorbed dose of 4 Gy for the untreated cells (Fig. S8, upper panel, ESI†). This effect was confirmed and further strengthened in the long-term clonogenic assay by comparing the effect at a dose of 1 Gy of X-rays in the presence of **CNC*-Au-Glc 5** vs. a dose of 2 Gy for the untreated cells (Fig. 3B upper panel, and Fig. S10 upper panels, ESI†). This confirms the possibility to use roughly half dose of X-rays to obtain the same radiotoxicity effect (Fig. 3B). Glyconanomaterials **5** and **6** resulted in different levels of radiotoxicity enhancement: **CNC*-Au-Glc 5** reached a DEF peak value of 1.82 at 10 µg mL^{-1} dosage whereas **CNC*-Au-Man 6** obtained a DEF of 1.65 at same dose (Table 1). This suggests a different suitability of particles to therapeutic effect enhancements. Moreover, the effect of **CNC*-Au-Glc 5** and **CNC*-Au-Man 6** treated cells and X-rays on MCF10A cells was also analyzed. Notably, a mild to no enhancement of radiotoxicity (Fig. 3B, Table 1, and Fig. S8–S10, ESI†) in both short and long-term assays was observed. All together these data support the efficacy of our technology in providing the precision delivery of the dose enhancement selectively in cancer cells.

Effect of the combination of X-rays and the glyconanomaterial CNC*-Au-Glc 5 on DNA integrity and repair

After X-rays treatment, cells can sense single and double strand breaks and activate an extremely fine-tuned repair response that will determine cells' own fate according to the extent and duration of the damage. To gain better insights into this phenomenon, we measured DNA damage upon X-rays irradiation and in the presence of glyconanomaterial **5**, first testing physical parameters of DNA integrity and fragmentation performing comet assay (Fig. 4A). Comet DNA showed a clear and dose dependent decrease in integrity when nanoparticles have been added to the X-ray irradiation treatment (Fig. 4A) at both 1 Gy and 2 Gy. Focusing on the broken DNA (comet tail) we observed an increase in the momentum, showing that the damaged portion of DNA is more fragmented in the presence of **5** than with the X-rays alone (Fig. 4B). It is worth noting that decreases in DNA integrity and tail momentum of 1 Gy in combination with **CNC*-Au-Glc 5** are comparable to the integrity and fragmentation of the 2 Gy alone.

We then looked at the phosphorylation of histone H2A-X, producing γH2AX[35] which plays a key role for the assembly of the DNA damage response (DDR) at the sites containing damaged
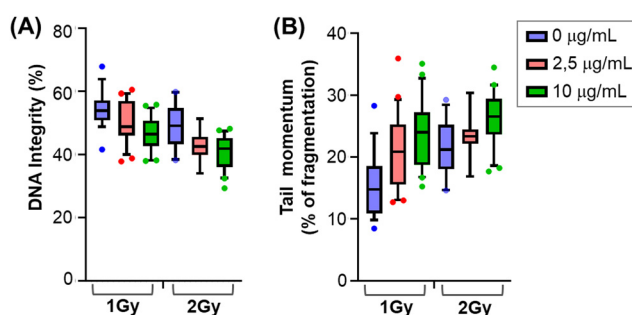
Fig. 4 MDA-MB-231 cells treated with **CNC*-Au-Glc 5** (0, 2.5, and 10 µg mL^{-1}) and X-rays (1 Gy and 2 Gy). (A) Evaluation of DNA integrity and (B) quantification of the comet tail momentum, representing the level of fragmentation of the damaged DNA. Graphs show the mean, 10–90 percentiles and individual values of outliers of twenty-one comets ($n = 21$).

chromatin as well as for activation of checkpoint proteins which arrest the cell cycle progression.[36] It is also important to consider that the cell cycle consists of a series of highly ordered, sequential phases that lead to cell division,[37] and there are checkpoints signaling activated in response to incomplete DNA replication and damaged DNA induced by both internal and external sources. One of the main DDR factors that induced cell cycle arrest is Chk1 (Checkpoint kinase 1).[38] Accordingly, we have investigated the level of γH2AX and pChk1 in cells treated and untreated with glyconanomaterial **5**, and exposed to X-rays, at different time points. In accordance with the previous literature,[39–41] we observed a moderate but an evident increase of both phosphorylation events in cells previously exposed to gold-loaded nanoparticles (Fig. S11, ESI†).

The results on DNA damage highlight the ability of **CNC*-Au-Glc 5** to increase chromatin fragmentation compared to X-rays alone, resulting in a stronger and prolonged activation of DDR markers. Due to its very tightly regulated nature, a moderate variation in DNA damage (DNA integrity and DDR activity) can result in a strong effect on cell viability and ability to proliferate, as resulted in the short- and long-term assays.

Conclusions

TNBC patients commonly undergo radiotherapy after surgery. However, some tumor cells develop radioresistance and around

30% of the patients experience tumor relapse within one year from the surgery/therapy.[42,43] The radiation dose is a crucial factor as X-rays affect not only cancer cells but also the surrounding healthy tissues. Therefore, the challenging tasks of withstanding radioresistance in TNBC, and of using a reduced X-rays dose to obtain a favorable trade-off in the therapeutic ratio (*i.e.* killing cancer cells while sparingly surrounding the healthy tissue) are of pivotal importance. In this work, AuNPs enhancing effects have been studied. We have been interested in the homing ability of the sugar heads on the CNC-AuNPs modified surface that makes a cellulose-based backbone nanomaterial a Trojan horse, ensuring massive accumulation of the Au radiosensitizer in TNBC. In our experiments, this approach resulted in augmenting radiotoxicity towards cells that had taken up the AuNPs compared to cells treated with only X-rays for all the X-ray's doses used. Therefore, here we provide a proof of concept of the efficacy of a glucose bearing hybrid programmable glyconanoplatform (CNC*-Au-Glc) as a radiotherapy enhancer for the treatment of this radioresistant cancer type. The tumor targeting strategy exploited by our nanotechnology impacts a hallmark of cancer, *i.e.* the GLUT channel overexpression that represents a metabolic fingerprint of cancer cells. This concept along with the robustness and reliability of our technology makes the CNC*-Au-Glc a suitable candidate as the nano-radiosensitizer in the treatment of radioresistant and challenging solid tumors, which could be employed for cancers other than TNBC.

Experimental

Experimental details and supplementary figures can be found in the ESI.†

Conflicts of interest

There are no conflicts to declare.

Notes and references

1 C. Fiorino, M. Guckenberger, M. Schwarz, U. A. Heide and B. Heijmen, *Mol. Oncol.*, 2020, **14**, 1500–1513.
2 J. M. Price, A. Prabhakaran and C. M. L. West, *Nat. Rev. Clin. Oncol.*, 2023, **20**, 83–98.
3 M. Reda, A. F. Bagley, H. Y. Zaidan and W. Yantasee, *Radiother. Oncol.*, 2020, **150**, 225–235.
4 K. Hintelmann, M. Kriegs, K. Rothkamm and T. Rieckmann, *Front. Oncol.*, 2020, **10**, 1260.
5 H. Shen, H. Huang and Z. Jiang, *Front. Pharmacol.*, 2023, **14**, 1145551.
6 J. H. Kim, K. A. Jenrow and S. L. Brown, *Radiat. Oncol. J.*, 2018, **36**, 172–181.
7 J. Park, Y. Choi, H. Chang, W. Um, J. H. Ryu and I. C. Kwon, *Theranostics*, 2019, **9**, 8073–8090.
8 Y. Y. Khine and M. H. Stenzel, *Mater. Horiz.*, 2020, **7**, 1727–1758.
9 E. Huynh and G. Zheng, *Wiley Interdiscip. Rev.: Nanomed. Nanobiotechnol.*, 2013, **5**, 250–265.
10 Z. Kuncic and S. Lacombe, *Phys. Med. Biol.*, 2018, **63**, 02TR01.
11 K. Haume, S. Rosa, S. Grellet, M. A. Śmiałek, K. T. Butterworth, A. V. Solov'yov, K. M. Prise, J. Golding and N. J. Mason, *Cancer Nanotechnol.*, 2016, **7**, 8.
12 N. M. Dimitriou, G. Tsekenis, E. C. Balanikas, A. Pavlopoulou, M. Mitsiogianni, T. Mantso, G. Pashos, A. G. Boudouvis, I. N. Lykakis, G. Tsigaridas, M. I. Panayiotidis, V. Yannopapas and A. G. Georgakilas, *Pharmacol. Ther.*, 2017, **178**, 1–17.
13 N. Goswami, Z. Luo, X. Yuan, D. T. Leong and J. Xie, *Mater. Horiz.*, 2017, **4**, 817–831.
14 D. B. Chithrani, S. Jelveh, F. Jalali, M. Van Prooijen, C. Allen, R. G. Bristow, R. P. Hill and D. A. Jaffray, *Radiat. Res.*, 2010, **173**, 719–728.
15 G. Biagiotti, G. Toniolo, M. Albino, M. Severi, P. Andreozzi, M. Marelli, H. Kokot, G. Tria, A. Guerri, C. Sangregorio, J. Rojo, D. Berti, M. Marradi, S. Cicchi, I. Urbančič, Y. van Kooyk, F. Chiodo and B. Richichi, *Nanoscale Horiz.*, 2023, **8**, 776–782.
16 P. Zagami and L. A. Carey, *npj Breast Cancer*, 2022, **8**, 95.
17 N. Harbeck and M. Gnant, *Lancet*, 2017, **389**, 1134–1150.
18 T. Kong, J. Zeng, X. Wang, X. Yang, J. Yang, S. McQuarrie, A. McEwan, W. Roa, J. Chen and J. Z. Xing, *Small*, 2008, **4**, 1537–1543.
19 G. D. Holman, *Biochem. J.*, 2018, **475**, 3511–3534.
20 E. Dalle Vedove, G. Costabile and O. M. Merkel, *Adv. Healthcare Mater.*, 2018, **7**, 1–19.
21 E. J. Foster, R. J. Moon, U. P. Agarwal, M. J. Bortner, J. Bras, S. Camarero-Espinosa, K. J. Chan, M. J. D. Clift, E. D. Cranston, S. J. Eichhorn, D. M. Fox, W. Y. Hamad, L. Heux, B. Jean, M. Korey, W. Nieh, K. J. Ong, M. S. Reid, S. Renneckar, R. Roberts, J. A. Shatkin, J. Simonsen, K. Stinson-Bagby, N. Wanasekara and J. Youngblood, *Chem. Soc. Rev.*, 2018, **47**, 2609–2679.
22 B. Muhitdinov, T. Heinze, A. Turaev, A. Koschella and N. Normakhamatov, *Eur. Polym. J.*, 2019, **119**, 181–188.
23 B. Hammouda, *Probing Nanoscale Structures – the sans Toolbox*, 2008, https://api.semanticscholar.org/CorpusID:139951325.
24 M. Uhlig, A. Fall, S. Wellert, M. Lehmann, S. Prévost, L. Wågberg, R. von Klitzing and G. Nyström, *Langmuir*, 2016, **32**, 442–450.
25 Y. Chevolot, C. Bouillon, S. Vidal, F. Morvan, A. Meyer, J.-P. Cloarec, A. Jochum, J.-P. Praly, J.-J. Vasseur and E. Souteyrand, *Angew. Chem., Int. Ed.*, 2007, **46**, 2398–2402.
26 H. B. Pfister, M. Kelly, F. Qadri, E. T. Ryan and P. Kováč, *Org. Biomol. Chem.*, 2019, **17**, 4049–4060.
27 S. Fedeli, P. Paoli, A. Brandi, L. Venturini, G. Giambastiani, G. Tuci and S. Cicchi, *Chem. – Eur. J.*, 2015, **21**, 15349–15353.
28 Y. Ma, H. Zhang, C. Chen, L. Liu, T. Ding, Y. Wang, D. Ma, X. Ling, X. Chen, J. Li, G. Zhong, G. Ru, L. Zhang and J. Tang, *Oncogene*, 2022, **41**, 1589–1599.
29 V. Bhat, S. Pellizzari, A. L. Allan, E. Wong, M. Lock, M. Brackstone, A. E. Lohmann, D. W. Cescon and A. Parsyan, *Crit. Rev. Oncol. Hematol.*, 2022, **169**, 103566.

30 R.-X. Huang and P.-K. Zhou, *Signal Transduct. Target. Ther.*, 2020, **5**, 60.

31 L. Gong, Y. Zhang, C. Liu, M. Zhang and S. Han, *Int. J. Nanomed.*, 2021, **16**, 1083–1102.

32 R. Schürmann, S. Vogel, K. Ebel and I. Bald, *Chemistry*, 2018, **24**, 10271–10279.

33 M. Hossain and M. Su, *J. Phys. Chem. C*, 2012, **116**, 23047–23052.

34 A. Subiel, R. Ashmore and G. Schettino, *Theranostics*, 2016, **6**, 1651–1671.

35 E. P. Rogakou, D. R. Pilch, A. H. Orr, V. S. Ivanova and W. M. Bonner, *J. Biol. Chem.*, 1998, **273**, 5858–5868.

36 T. T. Paull, E. P. Rogakou, V. Yamazaki, C. U. Kirchgessner, M. Gellert and W. M. Bonner, *Curr. Biol.*, 2000, **10**, 886–895.

37 S. J. Elledge, *Science*, 1996, **274**, 1664–1672.

38 N. Walworth, S. Davey and D. Beach, *Nature*, 1993, **363**, 368–371.

39 S. Jain, J. A. Coulter, A. R. Hounsell, K. T. Butterworth, S. J. McMahon, W. B. Hyland, M. F. Muir, G. R. Dickson, K. M. Prise, F. J. Currell, J. M. O'Sullivan and D. G. Hirst, *Int. J. Radiat. Oncol.*, 2011, **79**, 531–539.

40 K. Bromma, L. Cicon, W. Beckham and D. B. Chithrani, *Sci. Rep.*, 2020, **10**, 1–14.

41 K. Yogo, M. Misawa, H. Shimizu, T. Kitagawa, R. Hirayama, H. Ishiyama, H. Yasuda, S. Kametaka and S. Takami, *Nanomaterials*, 2022, **12**, 771.

42 G. Bianchini, J. M. Balko, I. A. Mayer, M. E. Sanders and L. Gianni, *Nat. Rev. Clin. Oncol.*, 2016, **13**, 674–690.

43 L. Yin, J.-J. Duan, X.-W. Bian and S. Yu, *Breast Cancer Res.*, 2020, **22**, 61.